RSC Advances

PAPER

View Article Online
View Journal | View Issue

Cite this: *RSC Adv.*, 2022, **12**, 4795

Core–shell structured Li–Fe electrode for high energy and stable thermal battery

Jaewook Shin, [ab] Hyeonmuk Kang,[a] Yongju Lee,[a] Sang Hyeon Ha[c] and EunAe Cho *[ab]

The thermal battery, a key source for powering defensive power systems, employs Li alloy-based anodes. However, the alloying increases the reduction potential of Li which lowers the overall working voltage and energy output. To overcome these issues, Li alloy must be replaced with pure Li. Utilizing pure Li requires a structure that can hold liquefied Li because the working temperature for the thermal battery exceeds the melting point of Li. The liquefied Li can leak out of the anode, causing short-circuit. A Li–Fe electrode (LiFE) in which Fe powder holds liquefied Li has been developed. In LiFE, higher Li content can lead to higher energy output but increases the risk of Li leakage. Thus, Li content in the LiFE has been limited. Here, we demonstrate a novel core–shell electrode structure to achieve a higher energy output. The proposed core–shell LiFE incorporates a high Li content core and a low Li content shell; high energy comes from the core and the shell prevents the Li from leakage. The fabricated core–shell structured electrode demonstrates the high energy of 9074 W s, an increase by 1.66 times compared to the low Li content LiFE with the conventionally used Li content (5509 W s).

Received 14th June 2021
Accepted 1st February 2022

DOI: 10.1039/d1ra04588a

rsc.li/rsc-advances

Introduction

As non-rechargeable primary batteries, thermal batteries are one of the essential energy sources for defensive power systems.[1] The main advantage of utilizing the thermal batteries is in their inert property during storage. Due to the nature of those defense applications, it is difficult to predict when the battery will discharge power. For the power system to be dependable, the battery must have extremely long and reliable storage life (Fig. 1a). The thermal batteries utilize various eutectic Li salts as the electrolyte. They stay in solid-state during storage in room temperature.[2] As the Li^+ cation diffusion in the solid-state is extremely slow, the thermal batteries are near completely inert during storage, due to the inherent property. In addition, to quickly respond to the military actions in emergency situations, the battery activation time should be only a few seconds. Owing to the relatively low melting temperatures of eutectic Li salts (300–400 °C), thermal batteries satisfy the requirement. During activation, typically temperatures increase above 400 °C and the eutectic Li salt electrolyte liquefies to be

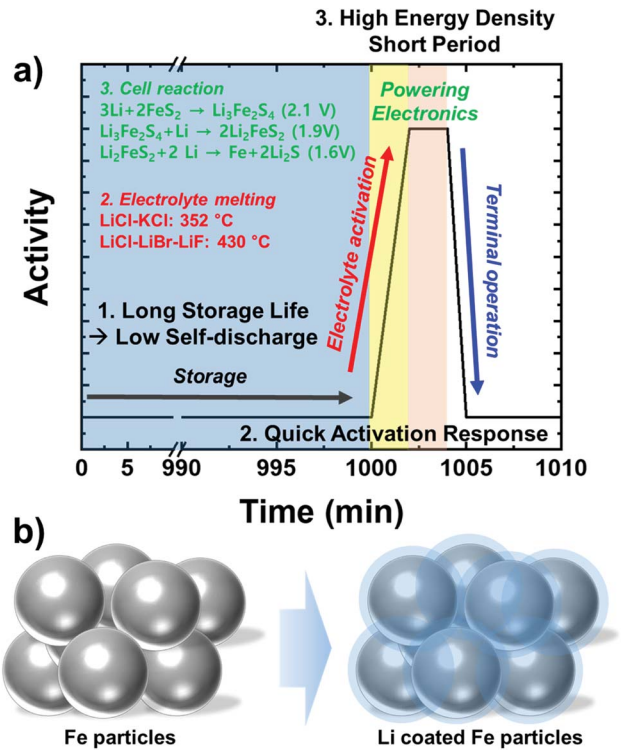

Fig. 1 (a) A graphical representation of the thermal battery operation. (b) A graphical illustration of the LiFE before and after Li incorporation.

[a]Department of Materials Science and Engineering, Korea Advanced Institute of Science and Technology (KAIST), 291 Daehak-ro, Yuseong-gu, Daejeon, 34141, Republic of Korea. E-mail: eacho@kaist.ac.kr; Tel: +82-42-350-3317

[b]Advanced Battery Center, KAIST Institute for NanoCentury, Korea Advanced Institute of Science and Technology (KAIST), 291 Daehak-ro, Yuseong-gu, Daejeon, 34141, Republic of Korea

[c]Agency for Defense Development, Yuseong P.O. Box 35-41, Daejeon, 34188, Republic of Korea

able to deliver Li^+ ions at a high rate. Once the battery is activated, it begins to power the electronics.

For the thermal battery anode, Li can be considered as the active Li source material. However, due to the low melting point of Li (180.5 °C), Li liquefies during activation, causing short-circuit by Li leakage and migration to the cathode side. As an alternative, Li–Si alloy or another type of Li alloys are utilized owing to their reliable physical state at the elevated operation temperature.[3] Li alloys utilized in the thermal batteries have a significantly higher melting point (Li–Si alloy T_m: 650–800 °C) that they remain solid-state during the thermal battery operation.[3] However, as the consequence of altering the electronic structure of Li by alloying, the anode reduction potential increases. Higher potential from the anode results in lower overall cell potential, thus lower energy output.

To mitigate the compromised output from the anode and to prevent short-circuit by Li leakage, Li electrodes with iron particles such as liquid anode network (LAN, by Aerospatiale Batteries (ASB)) have been proposed as an alternative anode system. The Li–Fe electrode (LiFE), first proposed in Catalytic Research Laboratory, is composed of Fe powder in Li matrix. Fe powder holds liquid Li during thermal battery operation. This system fully utilizes the thermodynamic potential of the Li because the Fe does not alloy with Li and the reduction potential of Li is unchanged. Thus, the Li–Fe electrode can produce higher full cell voltages than the conventional Li–Si alloys, owing to the lower reduction potential as an anode. However, to avoid short-circuit and gain reliability, a sufficient amount of Fe powder should be included in the LiFE and the Li composition must be low (Fig. 1b).[4–6] However, the low Li composition leads to low energy density. An innovative methodology must be incorporated to be able to utilize the LiFE system with high energy and power density.

In LiFE, the low Li composition anode has low energy but good reliability. The high Li composition anode has high energy but bad reliability. This work presents a core–shell type electrode design to combine the two types of Li composition. The newly proposed electrode brings out the benefits and mitigates the disadvantages from the low-Li and high-Li composition electrodes. We have implemented the high Li composition electrode as the core and low Li composition electrode as the shell. The core high-Li electrode may liquefy and become physically unstable, but the shell low-Li electrode will act as a barrier for liquid Li from escaping and causing short-circuit. In addition, owing to the high-Li core, the overall electrode has a high energy density. The core–shell LiFE is characterized by scanning electron microscopy (SEM), electrochemical discharge, and impedance electrochemical spectroscopy (EIS).

Experimental

Electrode preparation

The 13 wt% and 20 wt% LiFE were fabricated by first mixing 13 wt% of Li (MTI Korea) with Fe powder (H857) for the low-Li composition electrode and mixing 20 wt% of Li with Fe powder for the high-Li composition electrode. The mixing was done in Ar filled glovebox (oxygen level < 10 ppm, H_2O level < 0.1 ppm) at 350 °C with stainless steel beaker and spatula. At the elevated temperature, the Li was first melted and Fe powder was poured in the liquefied Li slowly under mechanical stirring. Upon reaching homogeneity, the Li–Fe mixture was scooped out onto a stainless steel plate and allowed to cool. The Li–Fe ingot was covered with polypropylene (PP) film and pressed with a hydraulic press down to ~3 mm thickness. Then it was roll pressed into 0.55 mm thickness slab for both 13 wt% LiFE and 20 wt% LiFE.

The core–shell LiFE was fabricated with the 13 wt% Li–Fe roll-pressed into 0.2 mm thickness slab and 20 wt% Li–Fe roll-pressed into 0.8 mm thickness slab. The 20 wt% Li–Fe slab was sandwiched in between the 13 wt% Li–Fe slabs. The sandwiched slabs were then roll pressed into 0.55 mm thickness as the core–shell LiFE.

To fabricate the prepared LiFEs into hollow-structured anodes of thermal battery, the rolled-out slabs (13 wt% LiFE, 20 wt% LiFE, and core–shell LiFE) were punched out using disks with 56 and 7.4 mm diameter, concentrically. The anode was then pressed with a Ni mesh sealed in a Ni cup. The Ni grid has diamond shape windows and 30 mesh count.

Characterization

Morphologies and structure of the Fe particles, 13 wt% and 20 wt% Li slabs were characterized by SEM (Philips XL30) and powder X-ray diffraction (PXRD, Rigaku Smartlab). The SEM samples were prepared and sealed under Ar environment and the seal was kept until being mounted onto the SEM chamber. The PXRD samples were prepared and sealed with caption tape under Ar environment and the patterns were obtained with the seal.

Full cell test

To test the electrochemical discharge energy, thermal battery full cell was fabricated with the prepared LiFE with excess amount of commercial cathode and electrolyte. The cathode was composed of 7.3 wt% of LiCl, 8.9 wt% of KCl, 8.8 wt% of MgO, 1.5 wt% of Li_2O and 73.5 wt% of FeS_2. The composition was mixed in a dry room (dew point < −40 °C) and pressed into a pellet with the same hollow area as the anode. 11.92 g of the cathode was utilized per electrochemical full cell to make sure that the discharge was anode limited. The electrolyte was composed of 12.1 wt% of LiCl, 37.6 wt% of LiBr, 5.3 wt% of LiF, and 45 wt% of MgO. The raw materials were purchased in battery grade and no further purification had been taken place. Purity of the salts were mostly above 98%. The composition was also mixed in the dry room and pressed into a pellet with the same hollow area as the anode. 2.48 g of electrolyte was utilized per electrochemical full cell. The full cell was stacked with anode–electrolyte–cathode and sandwiched between two sheets of gold-coated stainless steel plates.

The electrochemical discharge was performed with applied pressure at an elevated temperature. The assembled full cell was first pressed with 80 Kg F pressure with two hot plates (top and bottom). Once the desired pressed has been reached, the temperature of the hot plates was raised to 500 °C. Then, the

open-circuit voltage was measured for about 2 min and 8.89 A current was applied to the full cell until the voltage drops to ~0 V.

Electrochemical analyses

The electrochemical polarization and EIS tests were performed in a typical symmetrical cell. 1 M $LiPF_6$ in EC : DEC (ethylene carbonate : diethyl carbonate) (1 : 1 v/v) electrolyte (panaX etec) was utilized. Two disks (8.5 mm diameter) of the prepared appropriate LiFE, separator (Tonen), and the respective electrolyte were assembled in 2032 coin cell with a spring and spacer set (Wellcos) in an Ar-filled glovebox. The electrochemical cycling tests were conducted *via* constant current electroplating and electrostripping (WonATech Co., Ltd, WBCS3000L) with an applied current of 0.225 mA cm^{-2} for 1 hour each for the electroplating and electrostripping. After the first cycle, the symmetric cells were rested for 1 hour and their EIS were measured. The EIS measurements were obtained at the open circuit voltage with 10 mV voltage amplitude. The frequency range was 100 kHz to 0.01 Hz. The measurements were collected by using Autolab PGSTAT302N with Nova 1.11 software.

Results

To hold liquefied Li, Fe particles were mixed with the Li metal in the LiFE. Because Fe does not alloy with Li, it makes a suitable candidate to maximize energy density of the thermal battery. To first understand the morphology of the Fe particle used for fabricating LiFE, SEM images of as-purchased Fe powder are provided (Fig. 2a and b). The Fe morphology is composed of primary and secondary Fe particles. The secondary particles are as big as 10–20 μm in size and the primary particles are as small as 1–2 μm in size. The morphology of primary particles are largely irregular and have multiple edges. These small primary particles are agglomerated to form secondary particles, allowing good electrochemical contacts among Fe particles. Due to the irregular morphology of the primary particles, the secondary particles have many pores between the primary particles. The porous structure can likely assist in holding liquefied Li in the pores. Especially during the thermal battery operation, the irregular morphology and porosity can suppress mobility of the liquefied Li.

The core–shell structured LiFE was designed to be composed of 20 wt% LiFE core and 13 wt% LiFE shell. Recently, Im *et al.* in 2018 demonstrated that 13 wt% Li is the maximum amount of Li content without causing Li leakage in LiFE.[7] Thus, for the shell, 13 wt% Li LiFE is chosen to prevent Li leakage. For the core, to increase the energy density, 20 wt% Li LiFE has been employed. The optical images of the roll-pressed 13 wt% Li and 20 wt% Li slabs and step-by-step process of fabricating the core–shell LiFE are provided (Fig. 3). Fe powder was mixed with liquefied Li metal with 13 and 20 wt% Li. Then, the mixtures were poured into ingots, which were roll-pressed into slabs to obtain LiFE (Fig. 3a and b). Then, a 20 wt% LiFE was sandwiched with two slabs of 13 wt% LiFEs to form the core–shell structured electrode (Fig. 3c).

One of the key features of LiFE is the fact that the Li and Fe do not chemically react and hence the electronic structure of Li is unaltered. Unaltered Li state gives the lowest anode potential same as the pure Li and highest voltage output. To examine whether or not the Li and Fe chemically react to form other phases, PXRD patterns of Fe powder, 13 wt% Li LiFE, 20 wt% Li LiFE, and core–shell LiFE are obtained (Fig. 4a). All four samples show sharp peaks around 44.8° and 65.1° representing crystalline Fe phase and a broad peak around 18° representing the amorphous phase Kapton tape used to seal the samples to prevent from air contamination. The air can react with Fe and Li to form Fe_2O_3, Li_2O, and Li_3N.[8–10] The uncontrolled amount of these unwanted side products add inactive mass and volume, leading to lowering gravimetric and volumetric energy density. Because the PXRD patterns are measured with Cu K_α radiation, the Li metal phase cannot be detected.[11] No additional crystalline nor amorphous phase has been found. These results signify that even after mixing liquefied Li with Fe powder at an elevated temperature of 350 °C, Fe and Li did not react to form other phases and that the chemical state of Li has not been altered.

The SEM images of the 13 wt% Li LiFE and 20 wt% Li LiFE are obtained to better understand the electrode morphology (Fig. 4b and c). Both images show light contrasts in dark background. The light contrasts represent Fe particles coated with Li metal. The Li metal cannot be clearly imaged in the SEM because the Li atoms have very little interaction with e^- in the SEM.[12,13] The main difference between the 13 wt% Li LiFE and the 20 wt% Li LiFE is the spacing among the Fe particles. Because Li has a significantly lighter density (0.534 g cm^{-3}) than

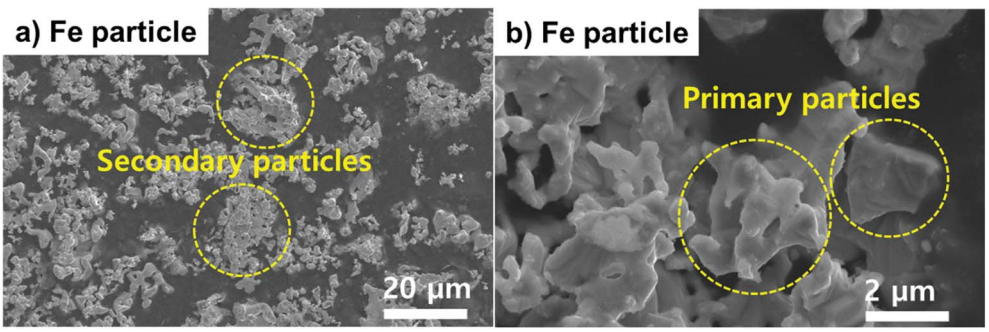

Fig. 2 (a and b) SEM images of the Fe particles.

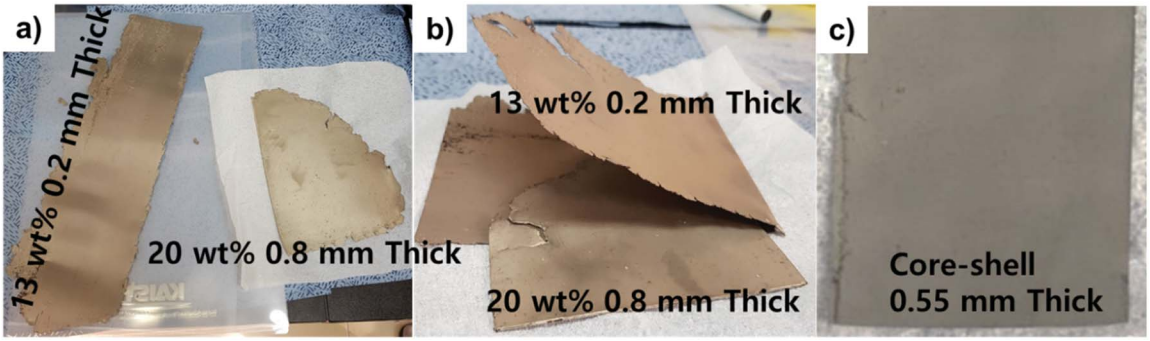

Fig. 3 (a) Optical images of the 13 wt% Li and 20 wt% Li slabs. (b) The fabrication process of the core–shell LiFE. (c) Prepared core–shell LiFE.

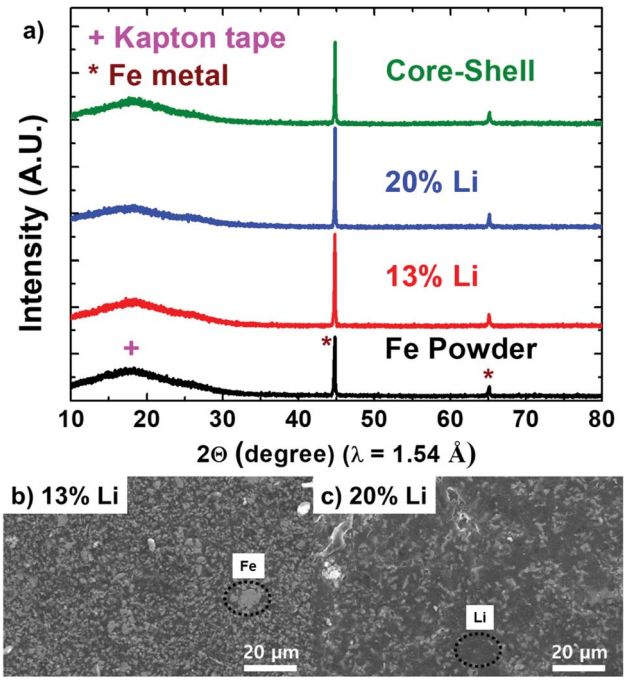

Fig. 4 (a) XRD patterns for the three LiFE and the Fe powder. SEM images of the (b) 13 wt% Li LiFE and (c) 20 wt% Li LiFE.

Fe (7.874 g cm^{-3}), in terms of volume, 13 wt% and 20 wt% Li composition correspond to 69 v% and 79 v%, respectively. Thus, the Fe volume is 31 v% and 21 v% in 13 wt% and 20 wt% LiFE, respectively. The spacing among the Fe particles in SEM represents the difference in the volumetric composition of Fe. The 13 wt% Li LiFE, compared to the 20 wt% Li LiFE has significantly more compacted Fe particle distribution. Such a compacted distribution likely has a better ability to hold liquefied Li in place and better electrical pathways through the connected Fe particles. Due to the less compacted Fe distribution, 20 wt% Li LiFE is more likely to have liquid Li leakage that leads to short-circuit and loss of active Li for electrochemical discharge.

Upon punching out the 0.55 mm thick LiFEs in hollow disks, the electrodes were weighed in a dry room (Table 1). All four electrodes have the same volume (1331 mm^3). As expected, 13 wt% Li LiFE has the highest electrode mass, followed by

Table 1 LiFE dimensions, masses, Li density, and theoretical capacity for the three LiFEs

	13 wt% Li LiFE	20 wt% Li LiFE	Core–shell LiFE
Electrode thickness (mm)	0.55	0.55	0.55
Electrode volume (mm^3)	1331	1331	1331
Electrode mass (g)	3.77	2.78	3.18
Active Li mass (g)	0.49	0.56	0.55
Specific Li mass (mg mm^{-3})	0.37	0.42	0.41
Theo. Cap. (A sec)	6841	7818	7679

core–shell LiFE and 20 wt% Li LiFE. Based on the mass of the electrodes, the overall Li content of the core–shell LiFE has been calculated to be 17.2 wt%. In thickness, the core–shell electrode is composed of 0.111 mm thick 13 wt% Li LIFE in the top and bottom layers and 0.328 mm thick 20 wt% Li LIFE core layer. Based on the electrode mass, the amounts of active Li available for the electrochemical discharge can be calculated; 13 wt% Li, 20 wt% Li, and core–shell LiFE have active Li mass of 0.37, 0.42, and 0.41 mg mm^{-3}, respectively. Compared to the 13 wt% Li LiFE, by incorporating the core–shell LiFE, the electrode mass has decreased by 16% but the active Li mass has increased by 11%. As a result, the theoretical capacity of each LiFE is 6841, 7818, and 7679 A s for 13 wt% Li, 20 wt% Li, and core–shell LiFE, respectively. These capacities are calculated based on the specific theoretical capacity of Li: 13 961 A s g^{-1}.

The punched out LiFEs were assembled into thermal battery anodes (Fig. 5a). The LiFE is first stacked and pressed with Ni mesh to hinder Li leakage. The pressed LiFE is then placed in a Ni cup and the edge of the cup was bent inward so that the Li leak does not occur from the edges. When the full thermal battery cell is assembled, the cell components are pressed together to improve the packing density and electrical contact. The anode along with the electrolyte and cathode pellets are stacked together in between a set of Au coated stainless steel current collectors (Fig. 5b). The FeS_2 is utilized as the cathode active material with 73.5 wt% composition and 26.5 wt% of electrolyte.[14–17] To maximize the effect of LiFE anode and minimize any error from the cathode, an excess amount of cathode was utilized; 11.92 g of cathodes which contain 8.76 g FeS_2 (45 427 A s capacity) is used. Since theoretical capacity of Li

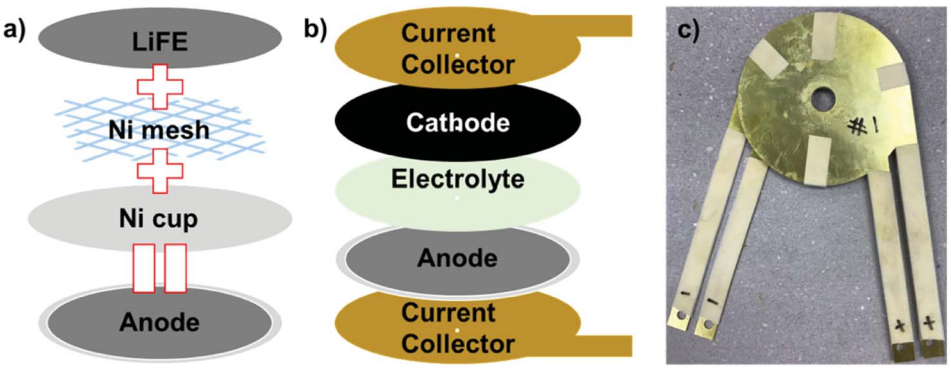

Fig. 5 (a) Schematic illustration of the thermal battery anode preparation. (b) Schematic illustration of the thermal battery assembly. (c) An optical image of the assembled thermal battery.

and FeS_2 is 13 961 and 5185 A s g^{-1}, respectively, capacity of the cathode is roughly 6 times the capacity of anodes. The electrolyte contains LiF–LiCl–LiBr eutectic salt with MgO as a binder. The eutectic salt has a melting point (~430 °C) lower than the thermal battery operation temperature, 500 °C. This salt is utilized to maximize the Li diffusion during the battery operation and for stable operation of the thermal battery. On the other hand, the MgO binder which does not melt during the battery operation was utilized to keep the structural integrity of the electrolyte during the battery operation. 2.48 g of electrolyte was utilized to ensure the structural integrity of the electrolyte pellet and minimize the Li^+ ion diffusion pathway. After all the thermal battery components have been stacked together, the full cell was held together by heat resisting tape (Fig. 5c).

13 wt% Li, 20 wt% Li, and core–shell LiFE anodes have been assembled into full thermal battery cells and their discharge performance has been measured (Fig. 6). During the discharge test, the full cells undergo three different phases: solid-state, liquid-state, and discharge. In the beginning, the prepared cell is at the solid-state. To measure their discharge performance, the full cells are heated to 500 °C, so that the electrolyte will liquefy. Once the electrolyte has been melted, the cells are in the liquid-state and open-circuit voltage (OCV) can be measured. The OCV represents the Gibbs free energy difference between the cathode and the anode and can be considered as a characteristic parameter for judging the state of discharge.[18] The OCV at the end of liquid state is 2.05 V, 1.97, and 2.06 V, for 13 wt% Li, 20 wt% Li, and core–shell LiFE, respectively (Fig. 6a, c and e). The core–shell LiFE has the highest OCV with 13 wt% LiFE close second. These two have a typical OCV for the LiFE anode and FeS_2 based cathode.[7] On the other hand, the OCV for the 20 wt% Li LiFE is significantly low compared to the other two. In addition, while the 13 wt% and core–shell LiFE electrodes have fairly stable OCV during the liquid-state, the 20 wt% LiFE electrode has a sudden drop in OCV around 20–30 s before the discharge phase. This sudden drop in the OCV is likely a result of a Li leakage that causes short-circuit. During the short-circuit, some portion of the Li and FeS_2 reacts with each other and become inactive for electrochemical discharge.[19] Such phenomenon is called self-discharge. Although the short-circuit only lasts for a few seconds, the OCV has gone down due to reaction between Li and FeS_2.

The cells were kept in the liquid-state for roughly 2 min. After the 2 min, the constant current was applied to measure discharge performance. Immediately after the current was applied, the voltage dropped to an onset potential of 1.91 V, 1.89 V, and 1.92 V for 13 wt% Li, 20 wt% Li, and core–shell LiFE, respectively (Fig. 6a, c and e). The core–shell LiFE and 13 wt% Li LiFE have higher onset potential than the 20 wt% Li LiFE. This trend is consistent with the OCV's. The onset potential for the 20 wt% Li LiFE is lowest due to the Li leakage. The soft short circuit causes the Li react with cathode materials that increases the overpotential. The constant current was applied continuously until the voltage has reached 1.5 V. The time for the cells to reach the 1.5 V represents the useable capacity. The duration is 360, 258, and 560 s which corresponds 3204, 2296, and 4984 A s capacity, for 13 wt% Li, 20 wt% Li, and core–shell LiFE, respectively (Fig. 6a, c, e, and Table 2). The core–shell LiFE has the highest capacity and the 20 wt% Li LiFE has the lowest capacity due to Li leakage. The leaked Li reacted and inactivated a significant portion of Li anode and FeS_2 cathode. The lack of available active materials leads to lower capacity. The 13 wt% Li LiFE's capacity is the baseline capacity where the Li leakage is prevented but has limited in capacity due to the lack of Li composition. On the other hand, the core–shell Li LiFE has 1.55 times the capacity as the 13 wt% Li LiFE. Such a substantial increase in capacity is coming from the high Li content core of the electrode. The core–shell LiFE not only has stable thermal battery operation but also has high capacity.

To determine the state of thermal batteries after discharge, optical images of the discharged cells are provided in Fig. 6b, d and f. Compared to the pristine state of the thermal battery (Fig. 5c), color changes can be observed. Generally, all cells have the heat resistant tape turning dark due to carbonization and the gold coated stainless steel current collector changing to reddish-orange due to oxidation of stainless steel. These changes are present in all three cells and deemed little significance to the electrochemical discharge performance. The important change can be observed in the 20 wt% Li LIFE. Center of the cell has been filled with black material. The spots of the

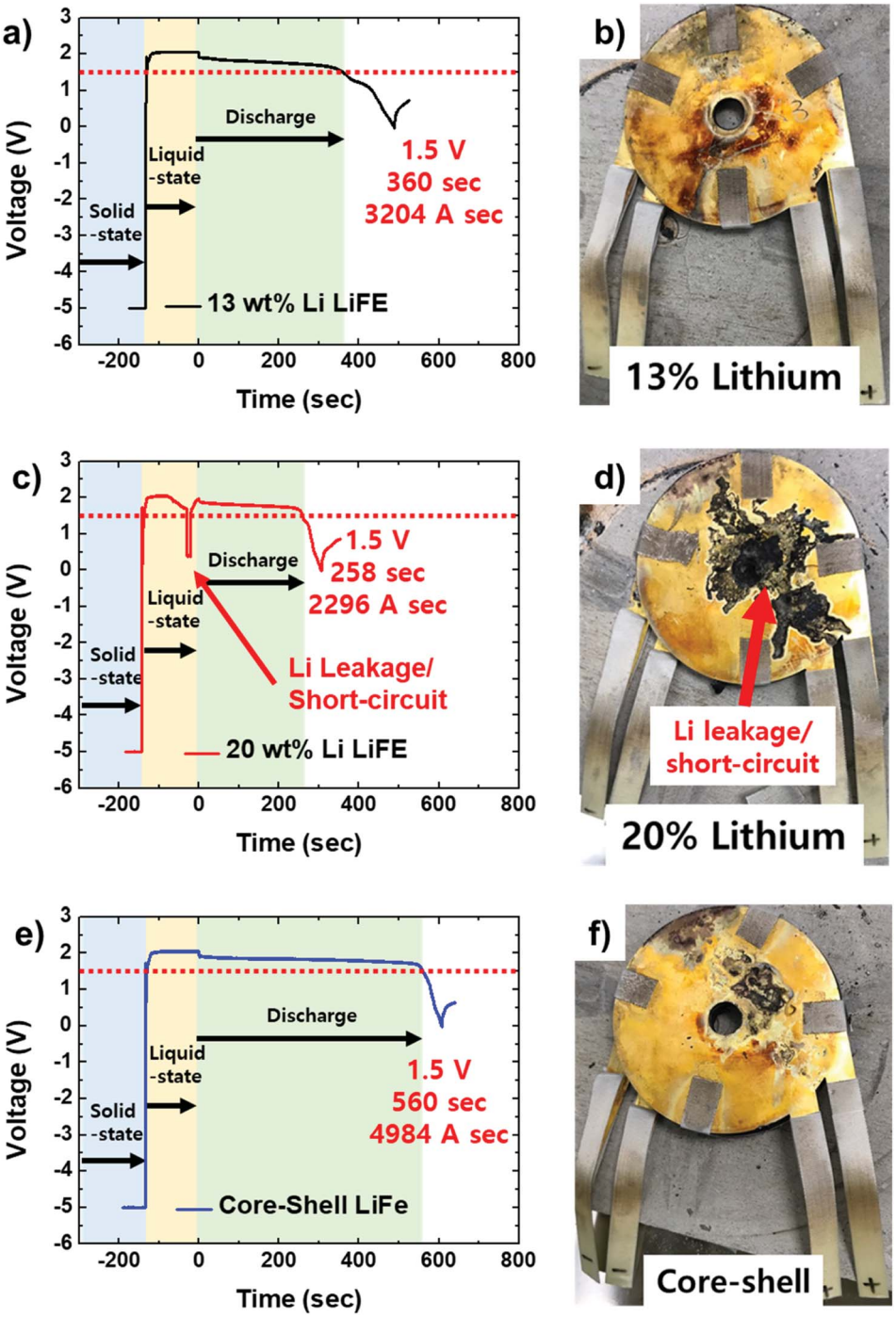

Fig. 6 Voltage profile of the (a) 13 wt% Li, (c) 20 wt%, and (e) core–shell LiFE cells above 1.5 V. Optical image of the electrochemically discharged thermal battery cell (b) 13 wt% Li, (d) 20 wt% Li, and (f) core–shell LiFE.

Table 2 Electrochemical discharging time, capacity, and yield for the three thermal battery cells

	13% Li	20% Li	Core–shell
Time@1.5 V (sec)	360 s	258 s	560 s
Cap. (A sec)	3204	2296	4984
Cap. Yield (%)	47	29	65

black material can be observed on the current collector as well. This black material is most likely a result of the Li leakage. During the liquid-state, Li from the 20 wt% Li LiFE leaked out and reacted with FeS_2. On the other hand, the other two LiFEs do not show any sign of such Li leakage. The absence of leakage further supports the stability of 13 wt% Li and core–shell LiFEs.

Besides the electrochemical discharge performance and the observation of Li leakage, further characterizations are

necessary to determine the electrode characteristics. The distribution of Fe has been observed under SEM. However, The Li distribution in LiFE is difficult to observe because Li atomic number is too low for the electron based microscopy techniques. To characterize Li morphology, electrochemical characterization techniques are proposed in this study (Fig. 7). First, expected Li morphologies are illustrated in Fig. 7a. During the mixing process between Li and Fe, liquefied Li mixes with Fe particles. When the Li solidifies, it forms a layer of Li coating on the Fe surface. In the low Li content electrode (13 wt% LiFE), the Li layer on the Fe surface will be thinner and more uniformly distributed. Due to such morphology, there will be more pores among the particles thus it has higher Li surface area. On the other hand, in the high Li content electrode (20 wt% LiFE), the Li layer on the Fe surface will be thicker and less uniformly distributed. Therefore, there will not be as many pores between the particles has lower Li surface area.

The surface area of Li was compared among the LiFEs by employing electrochemical techniques; electrochemical stripping and deposition technique and electrochemical impedance spectroscopy (EIS). For the electrochemical measurements, symmetric cells of the respective LiFEs with liquid organic electrolyte were assembled. Electrochemical stripping and deposition characteristics of Li in the organic electrolyte system is well known in the lithium-ion battery research.[20] During the deposition, Li deposits as a dendritic form. Due to the low reduction potential of Li, the organic electrolyte decomposes on the surface of Li and deposits as thick solid-electrolyte interphase (SEI), which is known to be highly resistive and impedes Li^+ ion diffusion.[21,22] On the surface of the dendrites, the electrolyte decomposition product, SEI forms. Electrochemically stripping the Li causes the dendrite to be detached from the Li and the detached dendrite becomes electrochemically isolated due to the insulating SEI layer. These detached Li is called "dead Li". Repeatedly depositing and stripping the Li generates more "dead Li". When more "dead Li" is formed on the Li surface, it causes increased electrochemical polarization and impedance. Given the same current density of electrochemical reactions, lower Li surface area will form larger dendrite. Thus, the dendrite is more likely to detach during electrochemical stripping. Lower Li surface area will have more "dead Li" formation, thus higher polarization and impedance. The degree of "dead Li" formation is inversely proportional to the Li surface area.

The polarization can be measured by observing the overpotential applied during the electrochemical deposition and stripping. 100 repeated electrochemical deposition and

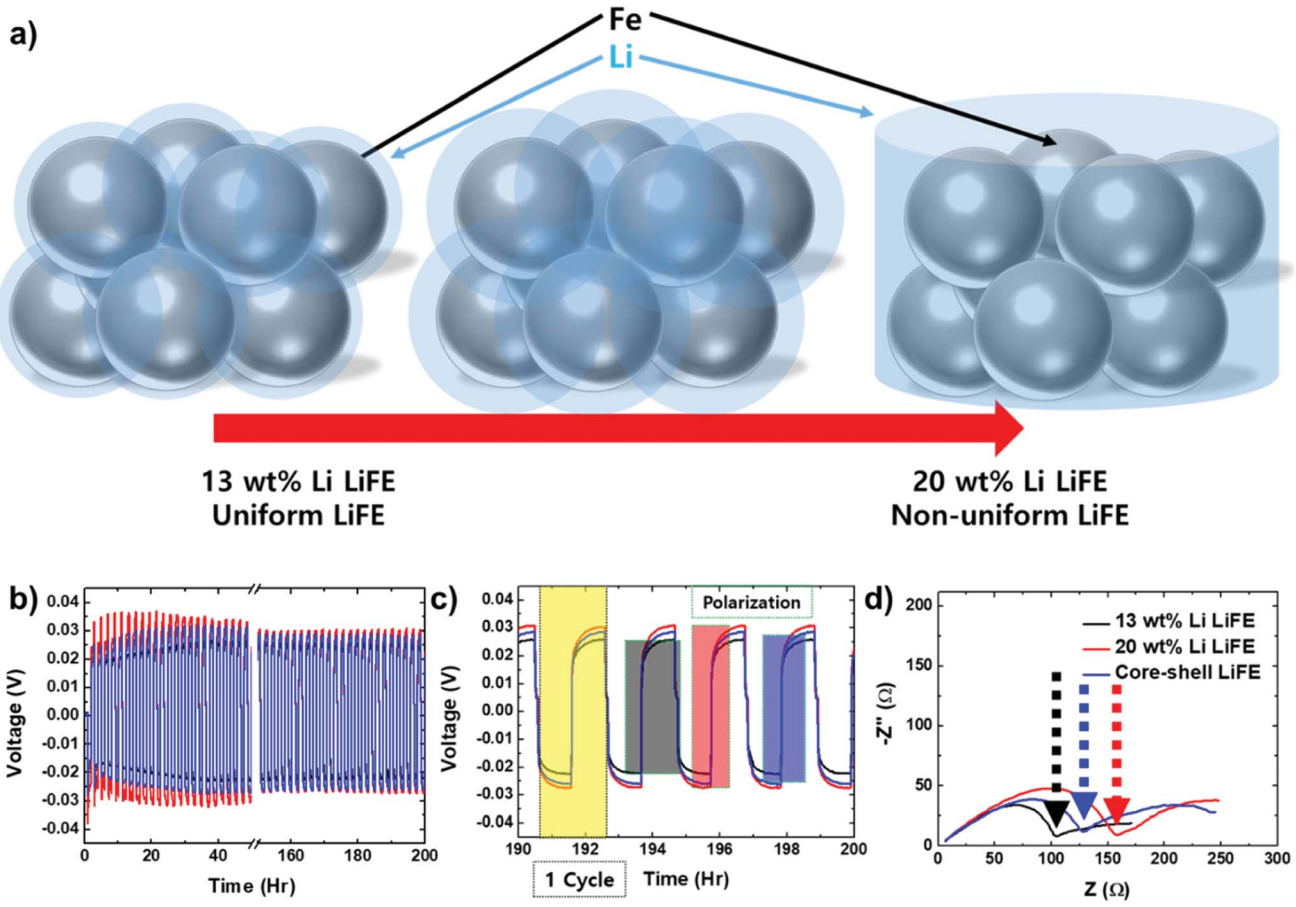

Fig. 7 (a) Schematic illustration of the Li coating morphology of LiFE depending on the Li content. (b) Electrochemical deposition and stripping cycle voltage profile of the three symmetric cells. (c) Zoomed-in electrochemical deposition and stripping cycle voltage profile of the three symmetric cells. (d) EIS of the three symmetric cells.

stripping cycles were performed on the symmetric cells (Fig. 7b). The polarization during the beginning of the repeated cycles varies, because of activation. The Li surface may have some amount of oxide that need to be activated and the bare Li surface gets covered with the SEI. The most amount of electrolyte decomposition, or formation of SEI, occurs during this activation period. After about 20 cycles (40 h), the polarization starts to stabilize. After 100 cycles (200 h), the polarization is fully stabilized. Throughout the cycles, the 20 wt% Li LiFE has the highest polarization. To observe the polarization more closely, the last five cycles are zoomed-in (Fig. 7c). During the deposition reaction the voltage increases and during the stripping reaction the voltage decreases. The polarization can be presented by ΔV:

$$\Delta V = V_{\text{stripping}} - V_{\text{depositing}} \quad (1)$$

where $V_{\text{stripping}}$ is the voltage at the end of stripping reaction and $V_{\text{depositing}}$ is the voltage at the end of the deposition reaction. The polarization is 48.2, 57.6, and 54.2 mV for 13 wt% Li, 20 wt% Li, and core–shell LiFE, respectively. As expected, the 20 wt% Li LiFE has the largest polarization and the 13 wt% Li LiFE has the smallest polarization. These indicate that the 20 wt% Li LiFE has smallest Li surface area and 13 wt% Li LiFE has largest Li surface area. The polarization and the Li surface area of the core–shell LiFE are in the middle of the other two LiFEs'. The core–shell LiFE is composed of high Li surface area 13 wt% Li (40.4%) and low surface area 20 wt% Li (59.6%). Combining the high and low surface area results in a medium surface area. In addition, since the polarization is also dependent on the current per active material, it is important to point out that the same amount of constant current has been applied regardless of the Li content. In terms of the current density, the 13 wt% Li LiFE should the highest polarization because it has the lowest amount of active Li. However, since the 13 wt% Li LiFE has the lowest polarization, it can be concluded that the lowest polarization originates from the large surface area.

In addition to the polarization, impedance can be measured to compare the Li surface area. Similarly, the impedance is also inversely correlated to the surface area.[23] The EIS has been measured for the assembled symmetric cells after one electrodeposition and electrostripping reaction cycle. During the electrochemical cycle, the electrolyte molecules start to decompose and form an insulating SEI layer on the Li surface. The amount of SEI layer is inversely proportional to the Li surface area. Measuring the Li^+ ion diffusion through the SEI layer allows for the comparison among the Li surface area. All three EIS spectra show a quasi-semicircle and Warburg impedance tail. The impedance at the end of the quasi-semicircle represents the Li^+ ion diffusion through the SEI layer. The impedance is 104, 159, and 128 Ω for 13 wt% Li, 20 wt% Li, and core–shell LiFE, respectively (Fig. 7d). As expected, the 13 wt% Li LiFE has the lowest impedance and 20 wt% Li LiFE has the highest impedance. These indicate that the 20 wt% Li LiFE has smallest Li surface area and 13 wt% Li LiFE has largest Li surface area. The core–shell LiFE has a medium amount of impedance because it contains both the high and low Li surface area. The impedance measurements show a consistent trend as the polarization measurement. This further supports and surface area of the Li in the respective LiFEs. Since having more Li surface area is correlated to having more uniform Li distribution, having uniform Li distribution helps to produce stable thermal battery operation.

Discussion

Based on the voltage profile provided in Fig. 6, the energy density of the three thermal batteries has been plotted (Fig. 8a). The energy density is 5509, 4054, and 9074 W s for 13 wt% Li, 20 wt% Li, and core–shell LiFE, respectively. Previously-reported capacity of a Li-impregnated metal foam anode was approximately 3000 As/g.[24] Since the energy density of the core–shell LiFE corresponds to a capacity of 9061 As/g, the core–shell LiFE is regarded to have an improved capacity. The 20 wt% Li LiFE, due to the Li leakage, has the lowest energy density. The core–shell LiFE has the highest energy density. The core–shell LiFE has about 1.65 times the energy density as the 13 wt% Li LiFE. Compared to 1.55 times for the capacity increase, the energy increase is more significant. This is because the average voltage for the core–shell is higher than that of the 13 wt% Li's. The average voltage above 1.5 V is 1.72, 1.77, and 1.82 V for 13 wt% Li, 20 wt% Li, and core–shell LiFE, respectively. Clearly, the average voltage for the core–shell LiFE is highest among the three batteries. This is because the core–shell LiFE has the lowest overpotential from polarization. Here, unlike in the electrochemical deposition and stripping cycle test, the

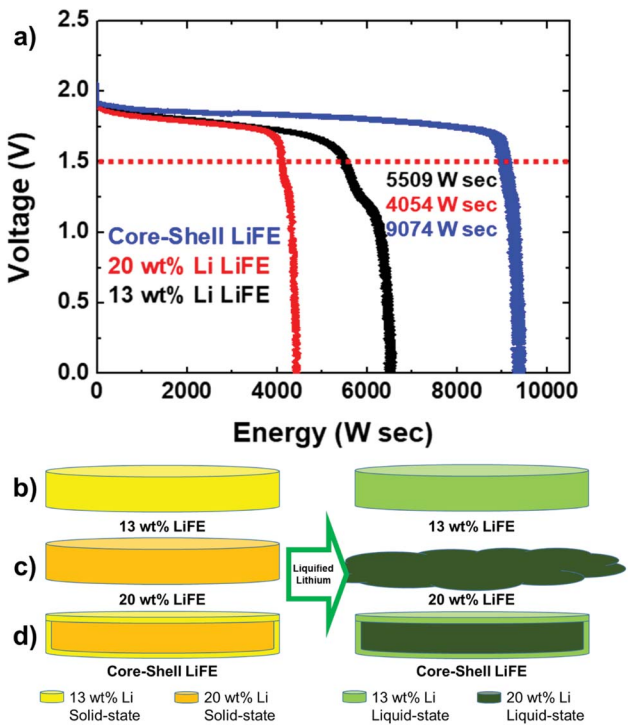

Fig. 8 (a) Energy density profile of the three LiFE cells above 1.5 V. (b–d) Schematic illustration of the three LiFE cells in solid- and liquid-state.

polarization is largely dependent on the amount of Li reaction per amount of Li, because the current density applied for the cycling test is substantially lower than that of the thermal battery discharge test. During the cycling test, roughly 0.1% of Li is involved in one hour. On the other hand, during the discharge test, roughly 50% of Li is involved in 5 min. The 20 wt% Li LiFE has higher average voltage than 13 wt% Li LiFE, but it only has 0.74 times the energy density as the 13 wt% Li LiFE (5509 *vs.* 9074 W s).

Based on the electrochemical discharge performance of the three thermal batteries, a schematic illustration of the LiFEs during thermal battery operation is provided (Fig. 8b and c). Before the thermal battery activation, all LiFEs are in solid-state. Upon activation, Li liquefies. When the Li liquefies, depending on the Li content, Li can remain in LiFE or leak out. In the 13 wt% low Li content, even when the Li is liquefied, the Li does not leak (Fig. 8b). However, it has limited energy density due to the low Li content threshold. On the other hand, in the 20 wt% high Li content, when the Li is liquefied, the Li leaks out and causes short-circuit (Fig. 8c). As a result, 20 wt% Li LiFE has even lower energy density than the 13 wt% Li LiFE. Lastly, to increase the energy density by increasing the Li content and to prevent Li leakage by decreasing the Li content, core–shell LiFE is fabricated. The core contains 20 wt% Li LiFE and the shell 13 wt% Li LiFE. The core may be unstable and Li may leak from the core, the Li does not leak out through the shell. By covering the 20 wt% Li with 13 wt% Li, the Li leak is prevented, even when the Li is liquefied (Fig. 8d).

Conclusion

It is clear that the 13 wt% Li content LiFE has good stability. However, due to the low Li content, it lacks energy density. Simply increasing the Li content to 20 wt% cannot increase the energy density because the Li leaks out under the thermal battery operation condition. The Li leakage causes short-circuit which results in even lower energy density than the low Li content LiFE. In order to increase energy density and retain stability, core–shell LiFE is proposed. The core–shell LiFE contains high Li content core and low Li content shell. The core provides high energy and the shell provides stability because the shell prevents Li from leaking. Consequently, the core–shell LiFE increases the energy density by 1.65 times compared to the low Li content LiFE. This work demonstrates a novel electrode configuration for thermal battery anode to both increase energy density and to retain stability. This study paves the way for exploring innovative electrode configurations to further energy density of the thermal battery.

Author contributions

J. S and H. K conceived the concept of the core–shell structured Li–Fe electrode. These authors equally contributed to this paper: J. S and H. K; J. S performed experimental planning, electrochemical measurement and characterization. H. K performed material synthesis, XPS, and data analysis, Y. L and S. H. H contributed to the experimental design and the discussion; J. S, H. K and E. A. C wrote the manuscript, and E. A. C supervised the project. All authors read and approved the final manuscript.

Conflicts of interest

There are no conflicts to declare.

Acknowledgements

The authors would like to thank the characterization facility in Department of Materials Science KAIST. This work was supported by the Agency for Defense Development (ADD) (UD170092GD).

References

1 R. A. Guidotti and P. Masset, Thermally activated (“thermal”) battery technology – Part I: An overview, *J. Power Sources*, 2006, **161**(2), 1443–1449.
2 P. Masset and R. A. Guidotti, Thermal activated (thermal) battery technology – Part II. Molten salt electrolytes, *J. Power Sources*, 2007, **164**(1), 397–414.
3 R. A. Guidotti and P. J. Masset, Thermally activated (“thermal”) battery technology – Part IV. Anode materials, *J. Power Sources*, 2008, **183**(1), 388–398.
4 G. C. Bowser and J. R. Moser, Molten metal anode, *US Pat.*, US3930888A, 1975.
5 D. Machado, S. Goldan, I. Londner and E. Jacobsohn, Fe–Li–Al anode composite and thermal battery containing the same, *US Pat.*, US7354678, 2008.
6 Y. S. Choi, H. R. Yu and H. W. Cheong, Electrochemical properties of a lithium-impregnated metal foam anode for thermal batteries, *J. Power Sources*, 2015, **276**, 102–104.
7 C. N. Im, H. K. Yoon, T. Y. Ahn, J. S. Yeo, S. H. Ha, H. R. Yu, S. Baek and J. H. Cho, Electrochemical properties of lithium anode for thermal batteries, *Appl. Chem. Eng.*, 2018, **29**(6), 696–702.
8 K. Park and J. B. Goodenough, Dendrite-Suppressed Lithium Plating from a Liquid Electrolyte *via* Wetting of Li_3N, *Adv. Energy Mater.*, 2017, **7**(19), 1700732.
9 K. Park, B. C. Yu and J. B. Goodenough, Li_3N as a Cathode Additive for High-Energy-Density Lithium-Ion Batteries, *Adv. Energy Mater.*, 2016, **6**(10), DOI: 10.1002/aenm.201502534.
10 D. W. Jeppson, J. L. Ballif, W. W. Yuan and B. E. Chou, *Lithium Literature Review: Lithium's Properties and Interactions*, H. E. D. Laboratory, 1978.
11 B. D. Cullity, *Elements Of X Ray Diffraction*, Addison-Wesley Publishing Company, Inc., 1956.
12 S. Yamashita, J. Kikkawa, K. Yanagisawa, T. Nagai, K. Ishizuka and K. Kimoto, Atomic number dependence of Z contrast in scanning transmission electron microscopy, *Sci. Rep.*, 2018, **8**, 12325.
13 P. G. T. Howell, K. M. W. Davy and A. Boyde, Mean atomic number and backscattered electron coefficient calculations for some materials with low mean atomic number, *Scanning*, 1998, **20**(1), 35–40.

14 D. R. Vissers, Z. Tomczuk and R. K. Steunenberg, A Preliminary Investigation of High Temperature Lithium/Iron Sulfide Secondary Cells, *J. Electrochem. Soc.*, 1974, **121**(5), 665–667.

15 P. J. Masset and R. A. Guidotti, Thermal activated ("thermal") battery technology – Part IIIa: FeS(2) cathode material, *J. Power Sources*, 2008, **177**(2), 595–609.

16 P. J. Masset and R. A. Guidotti, Thermal activated ("thermal") battery technology. Part IIIb. Sulfur and oxide-based cathode materials, *J. Power Sources*, 2008, **178**(1), 456–466.

17 S. Fujiwara, M. Inaba and A. Tasaka, New molten salt systems for high temperature molten salt batteries: Ternary and quaternary molten salt systems based on LiF–LiCl, LiF–LiBr, and LiCl–LiBr, *J. Power Sources*, 2011, **196**(8), 4012–4018.

18 R. F. Zhang, B. Z. Xia, B. H. Li, L. B. Cao, Y. Z. Lai, W. W. Zheng, H. W. Wang, W. Wang and M. W. Wang, A Study on the Open Circuit Voltage and State of Charge Characterization of High Capacity Lithium-Ion Battery Under Different Temperature, *Energies*, 2018, **11**(9), 2408.

19 W. M. Seong, K. Y. Park, M. H. Lee, S. Moon, K. Oh, H. Park, S. Lee and K. Kang, Abnormal self-discharge in lithium-ion batteries, *Energy Environ. Sci.*, 2018, **11**(4), 970–978.

20 C. Fang, X. Wang and Y. S. Meng, Key Issues Hindering a Practical Lithium-Metal Anode, *Trends Chem.*, 2019, **1**(2), 152–158.

21 J. Shin and E. Cho, Agglomeration Mechanism and a Protective Role of Al_2O_3 for Prolonged Cycle Life of Si Anode in Lithium-Ion Batteries, *Chem. Mater.*, 2018, **30**(10), 3233–3243.

22 J. Shin, T.-H. Kim, Y. Lee and E. Cho, Key functional groups defining the formation of Si anode solid-electrolyte interphase towards high energy density Li-ion batteries, *Energy Storage Mater.*, 2019, **25**, 764–781.

23 M. L. Tremblay, M. H. Martin, C. Lebouin, A. Lasia and D. Guay, Determination of the real surface area of powdered materials in cavity microelectrodes by electrochemical impedance spectroscopy, *Electrochim. Acta*, 2010, **55**(21), 6283–6291.

24 Y. S. Choi, H. R. Yu and H. W. Cheong, *J. Power Sources*, 2015, **276**, 102.